Supporting Information

N-doping WO_3 anchored on porous carbon as boosted oxygen reduction catalyst for zinc-air batteries

Jingwei Fang, Daijie Deng, Guorui Shi, Jinglei Fu, Wei Zhang*, Henan Li*, Shihan Zhang, Li Xu*

Institute for Energy Research, School of Chemistry and Chemical Engineering, School of Energy and Power Engineering, School of Foreign Languages, Jiangsu University, 212013 Zhenjiang, China

Email: wzhang@ujs.edu.cn; lhn@ujs.edu.cn; xulichem@ujs.edu.cn

Experiment reagent

Sodium tungsten dihydrate ($Na_2WO_4 \cdot H_2O$, ≥99%), chitosan($(C_6H_{11}NO_4)_n$, ≥99%), acetic acid (CH_3COOH, 99%), ethanol (C_2H_5OH, 99.7%), zinc acetate($Zn(CH_3COO)_2$, ≥99%), ammonium chloride (NH_4Cl, ≥99%), and potassium hydroxide (KOH, ≥99%) were obtained from Sinopharm Chemical Reagent Co., Ltd. (Shanghai, China). 1-Butyl-3-methylimidazolium Chloride ($C_8H_{15}ClN_2$, 99%) were obtained from Chengjie Chemical Co., Ltd. (Shanghai, China). Commercial Pt/C (20 wt.%) was procured from Alfa Assar Chemicals Co. Ltd. (Shanghai, China). Nafion (10 wt.%) was purchased from Sigma-Aldrich Chemie Gmbh (Shanghai, China). All experiments used self-made deionized water purified by Millipore system (Massachusetts, USA).

Apparatus

The phase and crystal structure of all samples were analyzed by X-ray diffractometer (XRD, Bruker 6100, Japan) with Cu Kα radiation (λ=1.5418 Å). X-ray photoelectron spectroscopy was adopted to study the information of element composition, chemical state, and chemical bond of various materials (XPS, ESCALAB 250 xl, Thermo VG Scientific, USA) at 1 kV. Field emission scanning electron microscope (SEM, JEOL-JSM-7800F) was used to study the fine structure of the material and analyze the microscopic composition. Transmission electron microscopy (TEM, Talos F200S) was used to study the fine structure of the material and analyze the microscopic composition. Raman spectrometer (Raman, RTS2) was used to detect the degree of graphitization and defects of the sample. Accelerated Surface Area and Porosimetry System (BET, Samsung II3020) was used to detect the pore structure and specific surface area of the sample. Fourier transform infrared spectroscopy (FT-IR, Nicolet iS50) is used to detect the material composition of the sample. Electrochemical measurements were performed on the CHI 760E workstation (CH instruments, Inc.) using a typical RRDE-3A rotator three electrode system. (Corresponding methods in supporting information).

Electrochemical Measurements

All the electrochemical measurements were controlled by CHI 760E electrochemical workstation (CHI Shanghai, Inc) with a standard three-electrode system. The Ag/AgCl

electrode (in a 3 mol L^{-1} KCl aqueous solution) and the platinum wire were served as the reference electrode and the counter electrode, respectively. The working electrode was the rotating disk electrode (RDE, diameter = 3 mm) and rotating ring disk electrode (RRDE, diameter of glassy carbon = 4 mm and diameter of platinum ring = 7 mm).

Preparing of working electrodes: 2 mg resultant electrocatalyst powder was dispersed in a mixed 402 μL Nafion/deionized water/ethanol (2 μL/200 μL/200 μL) solution and treated with ultrasound. 10 and 15 μL slurries were dropwise added onto cleaned RDE and RRDE surfaces, respectively. Then, the above RDE and RRDE electrodes were dried at room temperature, respectively. In contrast, RDE and RRDE electrodes modified by 20 wt% Pt/C were prepared with the same method.

The electrolyte of KOH (0.1 mol L^{-1}) was utilized throughout the entire test system. All potentials were converted to reversible hydrogen electrodes (RHE) with Eq. (1). The Koutecky-Levich plots (K-L) were calculated to evaluate ORR kinetics at different potentials range between 0.2, 0.3, 0.4, 0.5 and 0.6 V by linear fitting with Eq. (2). The electron transfer number (n) was evaluated by the slopes of K-L plots with Eq. (3).

$$E(\text{vs.}RHE) = E(vs.AgCl) + 0.059 \times \text{pH} + 0.197 \quad (1)$$

$$\frac{1}{j} = \frac{1}{j_k} + \frac{1}{B}\omega^{-1/2} \quad (2)$$

$$B = 0.2nF(D_{(O_2)})^{2/3} v^{(-1/6)} C_{(O_2)} \quad (3)$$

The measured current density and kinetic current density are respectively denoted by j and jk. F represents Faraday constant (F = 96485 C mol^{-1}). $D_{(O_2)}$ and $C_{(O_2)}$ are diffusion coefficient of the dissolved O_2 (1.86×10^{-5} cm^2 s^{-1}) and saturated O_2 concentration (1.21×10^{-6} mol cm^{-3}), respectively. ν and ω are the kinetic viscosity (0.01 cm^2 s^{-1}) and the rotation speed of electrode (r min^{-1}) of RDE, respectively.

The electron transfer number (n) and hydrogen peroxide (HO_2^-) yield of N-WO_3/PNC, WO_3/PNC, PNC and 20 wt% Pt/C during ORR were measured by RRDE electrodes and calculated by Eq. (4) and (5). The ring potential was kept at 1.25 V (vs. RHE).

$$n = 4I_d / (I_d + I_r / N) \quad (4)$$

$$HO_2^-(\%) = 200(I_r / N) / (I_d + I_r / N) \quad (5)$$

N is the current collection efficiency of Pt ring, which is determined to be 0.37. I_d and I_r represent the disk current and the ring current, respectively.

At the rotating speed of 1600 r min^{-1} (rpm), the stability of N-WO_3/PNC, WO_3/PNC, PNC and 20 wt% Pt/C were elevated for up to 10 h by the current-time (i-t) chronoamperometric response tests with the rotation speed of 1600 rpm and a sweep rate of 10 mV s^{-1} in 0.1 mol L^{-1} O_2-saturated KOH.

To estimate the electrochemical active surface area (ECSA) of catalytic surface through RDE, the electrochemical double layer capacitances (C_{dl}) in the non-Faradaic potential region were obtained by Eq. (6) derived from changing CV curves at the scan rates range between 2, 5, 10, 15, 20 and 25 mV s^{-1}.

$$ECSA = C_{dl} / C_s \quad (6)$$

Where C_{dl} = IC/ν. IC is the sum of charging/discharging at 1.015 V vs. RHE from different CV curves. The ν represents the scan rate. C_S is the capacitance of electrocatalytic materials on the smooth surface in the same electrolyte or specific capacitance of the catalysts.

Liquid zinc-air battery Measurement

To assemble zinc-air batteries, the slurry of N-WO_3/PNC, WO_3/PNC, PNC and 20 wt% Pt/C was dropwise added onto a carbon cloth with an area of 1 cm^2 to ensure a loading amount of 1 mg cm^{-2} as the air cathode. The polished zinc plate was used as the anode. The mixed solution of 6 mol L^{-1} KOH and 0.2 mol L^{-1} $Zn(CH_3COO)_2$ was the electrolyte solution. The charging and discharging polarization curves were measured by LSV polarization curves with a scan rate of 10 mV s^{-1}, and calculated the power density by Eq. (7):

$$\text{power density} = \text{current density} \times \text{voltage} \quad (7)$$

The galvanostatic (15 mA cm^{-2}) discharging curves was measured and calculated the specific capacity by Eq. (8):

$$\text{specific capacity} = \frac{\text{current} \times \text{test hours}}{\text{consumed zinc plate mass}} \quad (8)$$

Charging/discharging cycle polarization curves were tested on a NEWARE battery testing system BTSClient80 (current density: 10 mA cm^{-2}). Each charge-discharge cycle stability was tested with a cycle period of 20 min (10 min for charging and 10 min for discharging).

Quasi-solid Zinc-air cell measurement

To assemble zinc-air batteries, the slurry of N-WO_3/PNC, WO_3/PNC, PNC and 20 wt% Pt/C was dropwise added onto a carbon cloth with an area of 3.75 cm^{-2} to ensure a loading amount of 1.5 mg cm^{-2} as the air cathode. The polished zinc plate was used as the anode. The electrolyte was polyacrylamide organic hydrogel. The charging and discharging polarization curves were measured by LSV polarization curves with a scan rate of 10 mV s^{-1}, and calculated the power density by Eq. (6).

The galvanostatic (5 mA cm^{-2}) discharging curves was measured and calculated the specific capacity by Eq. (7).

Charging/discharging cycle polarization curves were tested on a CHI 760E electrochemical workstation (CHI Shanghai, Inc) (current density: 5 mA cm^{-2}). Each charge-discharge cycle stability was tested with a cycle period of 4 min (2 min for charging and 2 min for discharging).

Synthetic methods

The synthesis of N-WO_3/PNC: First, 0.5 mmol of 1-butyl-3-methylimidazolium chloride and 0.2 mmol of sodium tungstate were dissolved in 20 mL of deionized water, heated to 60 °C, mixed for 6 hours, then dried to obtain tungsten-based ionic liquid. Next, 0.3 g of chitosan was dispersed in 30 mL of deionized water and stirred for 30 minutes. Following this, 0.2 mmol of the tungsten-based ionic liquid was introduced, followed by the slow addition of 300 μL of acetic acid. The mixture was then stirred for another 0.5 hours to form a gel. Then it was transferred to the ball mill tank and 3 g ammonium chloride was added to the ball mill for 0.5 h to obtain the precursor. The chitosan aerogel was obtained after freeze-drying the precursor. The aerogel was placed in a covered crucible inside a quartz tube with one end closed. After tightening the flange, the air in the quartz tube was extracted using a vacuum pump. The quartz tube was then calcined in a muffle furnace at 950 °C for 10 minutes. After calcination, the quartz tube was immediately taken out and placed in a fume hood to cool down. Once cooled to room temperature, black powder was obtained. The powder was dispersed in 3 mol L^{-1} KOH solution, heated and stirred for 24 h. Then the powder dried under vacuum at 60 °C. The black powder obtained after drying under vacuum was placed in a covered crucible, and then placed in a quartz tube with one end closed. Then, the quartz tube

was calcined at 800 ℃ with the above method. After 10 min. the quartz tube was immediately taken out and cooled to room temperature, then, the N-WO_3/PNC catalyst can be obtained.

The synthesis of WO_3/PNC, PNC:

The synthesis methods of WO_3/PNC, PNC and N-WO_3/NC were like that of the N-WO_3/PNC, except that 1-butyl-3-methylimidazolium chloride and sodium tungstate were not added, respectively.

Computational details

All density functional theory (DFT) calculations were achieved with Vienna ab-initio simulation package (VASP 6.0) with the projector augmented wave pseudopotentials (PAW) to describe the interaction between atomic cores and valence electrons. A vacuum space of 15 Å was added in the z-direction. The Brillouin zone integrations were performed with a Gammacenter 3×3×1 k-point mesh for geometry optimization. The energy cut-off of the plane wave basis was set as 350 eV. During the geometry optimization, the energy change criterion was set to 1×10^{-5} eV, and the maximum force was 0.05 eV $Å^{-1}$. All the atoms in the model were relaxed until reaching the convergence criteria.

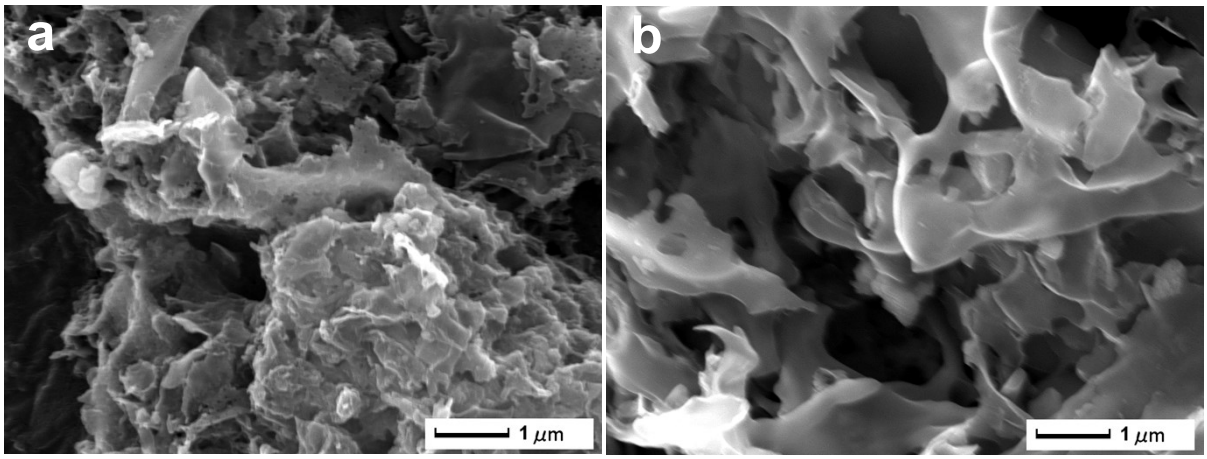

Fig. S1. SEM images of (a) the WO_3/PNC and (b) PNC.

The PNC also exhibits a fluffy morphology, which is different from the morphology of the WO_3/PNC catalyst.

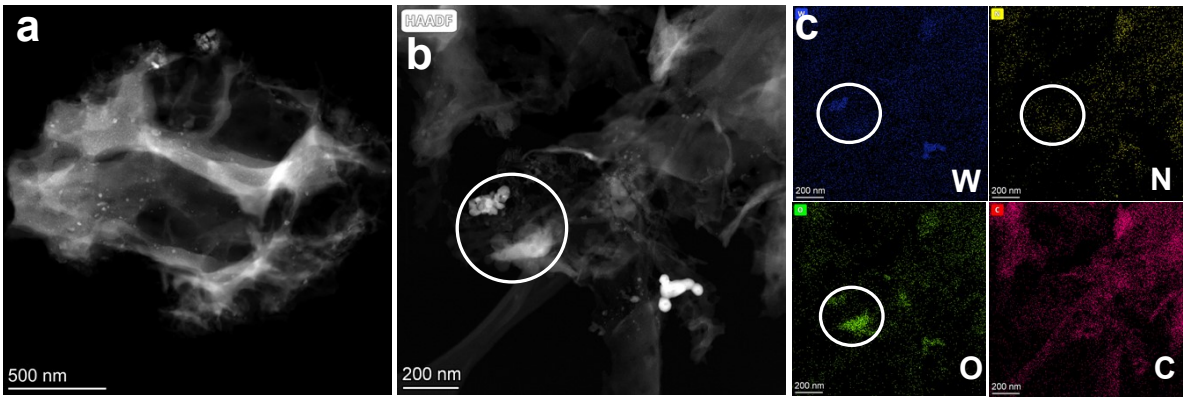

Fig. S2. (a, b) TEM images and (c) corresponding elemental mapping of the WO_3/PNC.

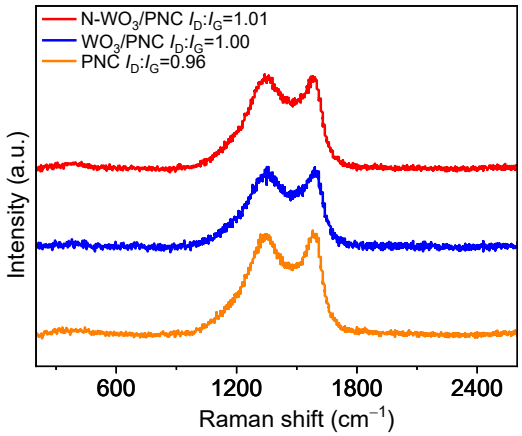

Fig. S3. Raman spectra of N-WO_3/PNC, WO_3/PNC and PNC.

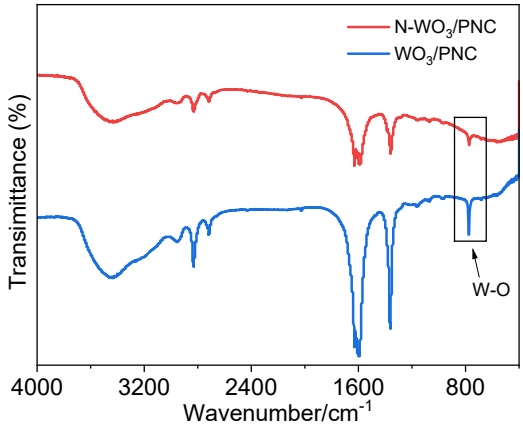

Fig. S4. FI-TR spectra of N-WO_3/PNC and WO_3/PNC.

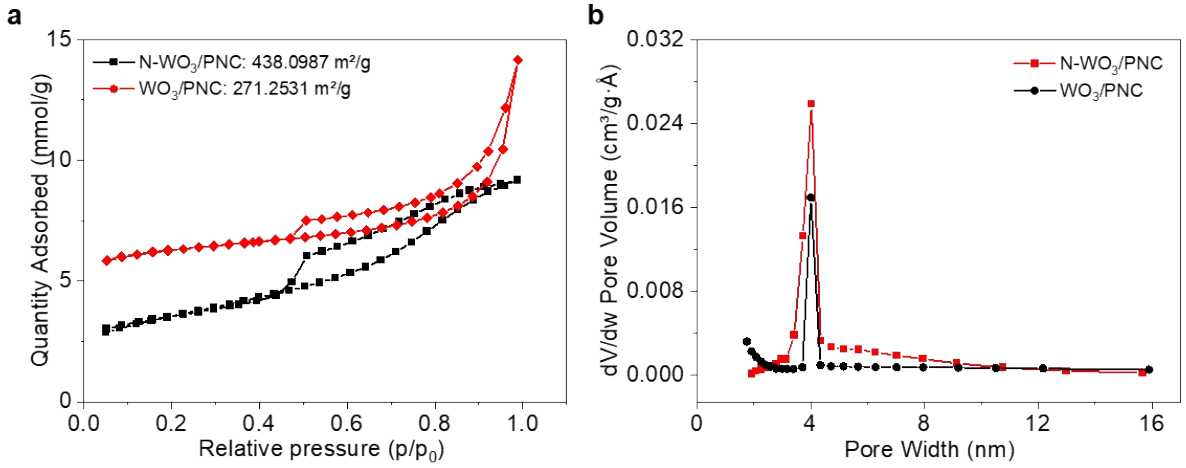

Fig. S5. (a) N_2 adsorption-desorption isotherms and (b) the corresponding pore size distribution of N-WO_3/PNC and WO_3/PNC.

To confirm the specific surface area and pore structure of N-WO_3/PNC, N_2 adsorption-desorption isotherms and the corresponding pore size distribution of N-WO_3/PNC and WO_3/PNC were carried out. The specific surface area of N-WO_3/PNC is 438.0987 m^2 g^{-1} (Fig. S5a). And, the average pore size is 4.12 nm (Fig. S5b). However, the WO_3/PNC synthesized without the addition of ionic liquid exhibits a specific surface area of 271.2531 m^2 g^{-1} and an average pore size of 4.05 nm. The addition of ionic liquid can not only form N doped WO_3, but also improve the specific surface area and pore structure of N-WO_3/PNC. The large number of pores in N-WO_3/PNC facilitates the diffusion of oxygen, which accelerates the ORR process.

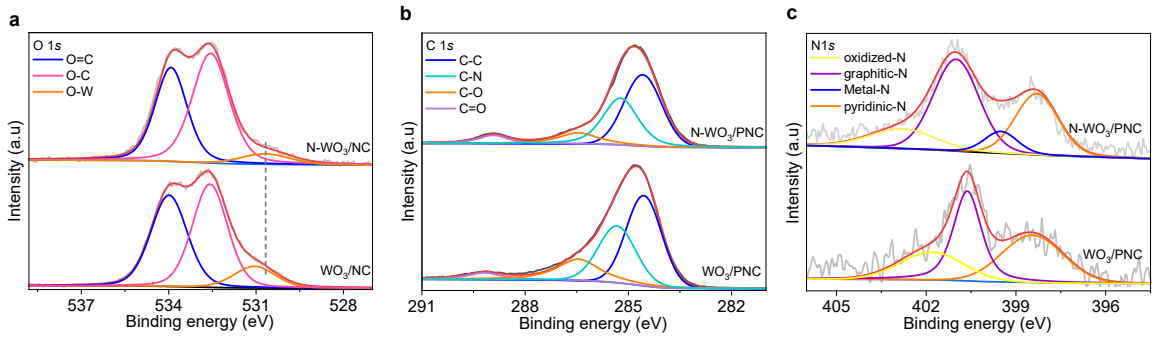

Fig. S6. (a) O 1*s*, (b) C 1*s* and (c) N 1*s* spectra of N-WO_3/PNC and WO_3/PNC.

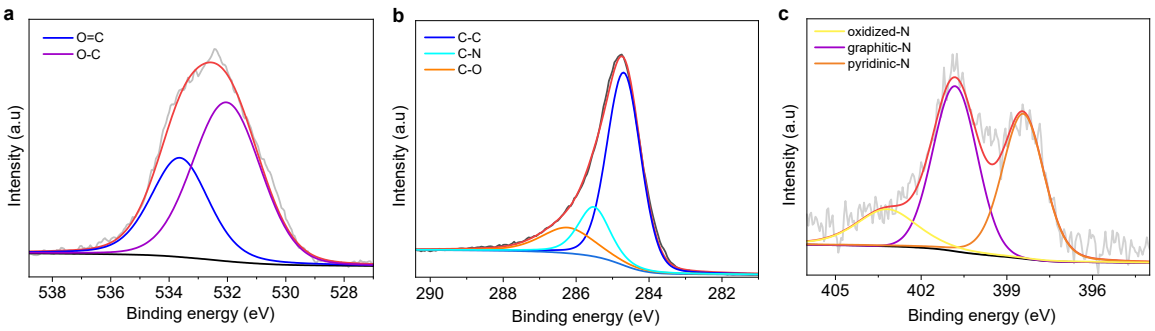

Fig. S7. XPS spectra of PNC: (a) O 1*s*, (b) C 1*s* and (c) N 1*s* spectra.

The obvious C=O and C−O characteristic peaks are fitted in O 1*s* XPS spectrum of the PNC (Fig. S7a). C 1*s* XPS spectrum of the PNC (Fig. S7b) are fitted to four characteristic peaks of C−C, C−N and C−O species. N 1*s* XPS spectrum of the PNC (Fig. S7c) demonstrates the simultaneous presence of pyridinic-N, graphitic-N, and oxidized-N.

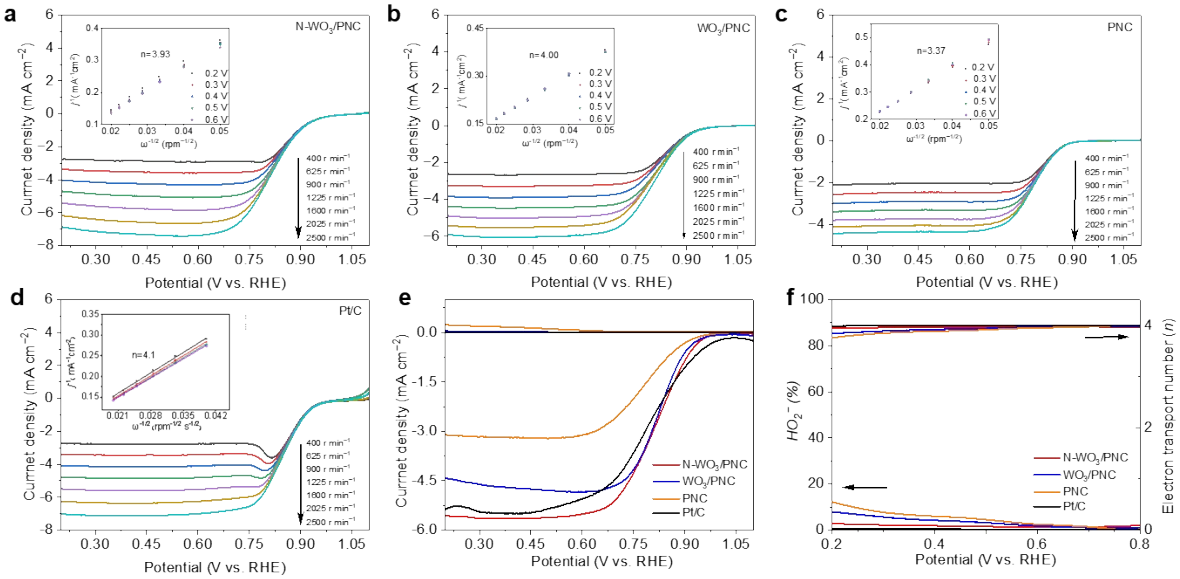

Fig. S8. LSV curves of (a) N-WO_3/PNC, (b) WO_3/PNC, (c) PNC and (d) Pt/C at different rotation speeds range of 400 - 2500 rpm (inset shows the corresponding K-L plots). (e) RRDE test of N-WO_3/PNC, WO_3/PNC, PNC and Pt/C. (f) The corresponding electron transfer number (*n*) and HO_2^- production rate.

Koutecky-Levich (K-L) plots results of the N-WO_3/PNC demonstrate an average electron transfer number of approximately 3.93 (Fig. S8), suggesting the ideal four-electron transfer pathway for oxygen reduction.

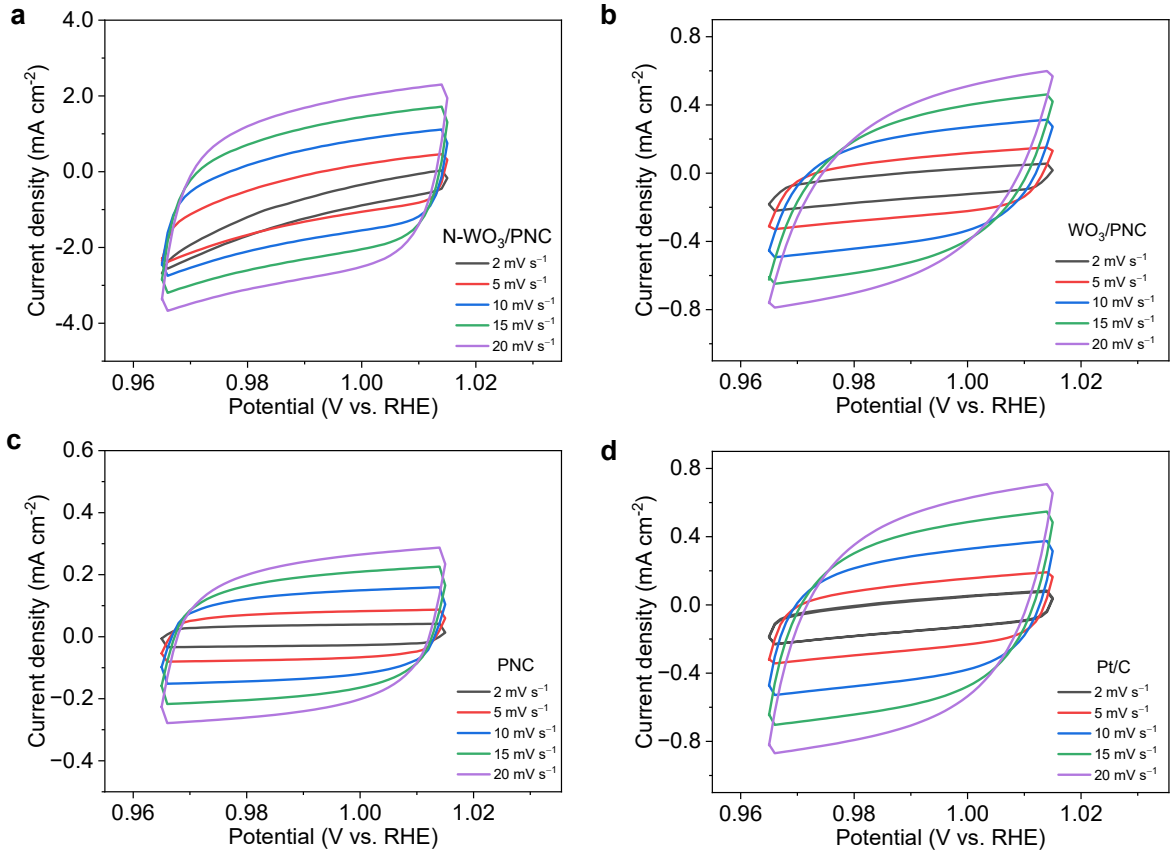

Fig. S9. CV curves of (a) N-WO_3/PNC, (b) WO_3/PNC, (c) PNC and (d) Pt/C.

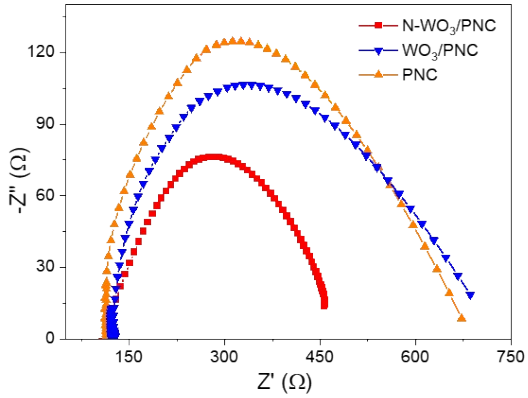

Fig. S10. Nyquist diagrams of N-WO_3/PNC, WO_3/PNC and PNC.

Nyquist diagrams provide information on the electron transfer properties of the of N-WO_3/PNC, WO_3/PNC and PNC during ORR. The small radius of the Nyquist plot indicates that the electron transfer resistance of N-WO_3/PNC is lower than that of WO_3/PNC and PNC. The smaller electron transfer resistance is beneficial to increase the overall ORR activity of the N-WO_3/PNC catalyst.

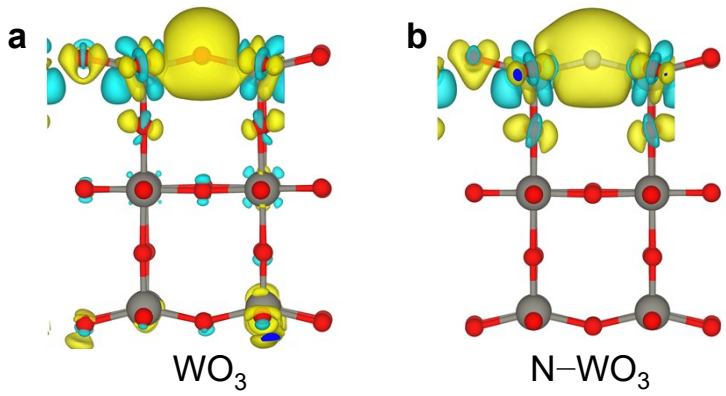

Fig. S11. Difference charge density of (a) WO_3 and (b) N-WO_3 (electron depletion: blue area, electron accumulation: yellow area).

The difference charge distribution of WO_3 and N-WO_3 was calculated. The WO_3 and N-WO_3 obvious charge distribution difference characteristics. This result represents that doped N atoms can promote the charge redistribution of WO_3, and then regulate its adsorption/desorption energy for oxygen-containing species.

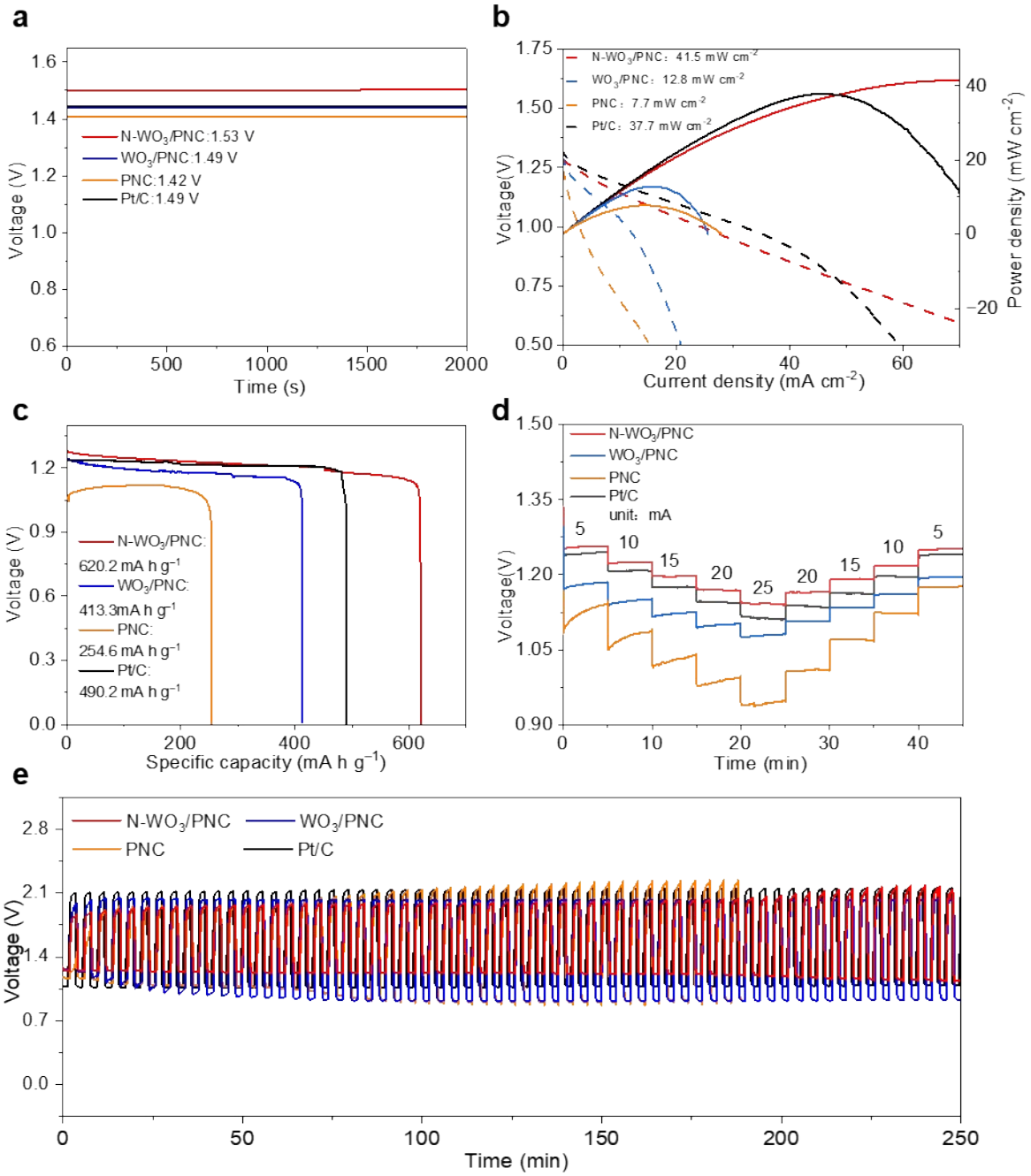

Fig. S12. Performances of quasi-solid ZABs with N-WO_3/PNC, WO_3/PNC, PNC and Pt/C as air-cathode catalysts: (a) open circuit voltage curves, (b) discharge curves and power density, (c) specific capacity curves at 5 mA cm^{-2}, (d) rate performances and (e) galvanostatic charge-discharge cycle curves of Zn-air batteries at 5 mA cm^{-2}.

Table S1. Comparison of ORR catalytic activity and kinetic performance for N-WO_3/PNC with some reported catalysts.

Catalyst	Half-wave potential (V vs. RHE)	Tafel slop ($mV\ dec^{-1}$)	Reference
N-WO_3/PNC	0.85	65.7	This work
NiFe/$W_{0.3}C$@NC	0.81	61	[3]
WNPc/gC_3N_4-700	0.83	40.4	[4]
W-N-C	0.86	71	[5]
WN-n	0.73	76	[6]

Table S2. Comparison between N-WO_3/PNC with some reported materials as air-cathode catalysts in liquid zinc-air batteries.

Catalyst	Power density ($mW\ cm^{-2}$)	Specific capacity ($mA\ h\ g^{-1}$)	Cycling time (h)	Reference
N-WO_3/PNC	209.7	790.1	250 (10 $mA\ cm^{-2}$)	This work
FeCo-WC/NC	122.52	744	200 (5 $mA\ cm^{-2}$)	[7]
5%Pd/$WO_{2.72}$	168	633	/	[8]
FeCu-BTC/WO_3-WC	135.2	551	300 (5 $mA\ cm^{-2}$)	[9]
W-Co_2P/NC	224.4	881	130 (10 $mA\ cm^{-2}$)	[10]

Reference

[1] Y. Zhao, H. Chen, X. Ma, J. Li, Q. Yuan, O. Zhang, M. Wang, J. Li, M. Li, S. Wang, H. Guo, R. Hu, K. Tu, W. Zhu, X. Yang and Y. Pan, Advanced Materials, **2023**, 36, 230243.

[2] Z. Wang, D. Deng, H. Wang, S. Wu, L. Zhu, L. Xu and H. Li, Journal Colloid Interface Science, **2024**, 653, 1348-1357.

[3] E. Jang, J. Cho, J. Kim and J. Kim, Applied Surface Science, **2024**, 663, 160201.

[4] C. Zhou, W. Ahmad, L. Yan, C. Qian, M. Ling, L. Zheng and S. Zhou, Cell report physical science, **2023**, 4, 101288.

[5] B. Jiang, H. Sun, T. Yuan, W. He, C. Zheng, H. Zhang, J. Yang and S. Zheng, Energy &

Fuels, **2021**, 35, 8173–8180.

[6] C. Zhang, H. Liu, C. Jin and H. Guo, Materials Letters, **2021**, 291, 129433.

[7] L. Xu, S. Wu, D. Deng, J. Qian, G. Lu and H. Li, Journal of Alloys and Compounds, **2021**, 868, 159236.

[8] Z. Yang, N. Jiang, S. Bei, K. Bao, M. Xiang, C. Yu, S. Dong and H. Qin, Electrochimica Acta, **2024**, 476, 143768.

[9] D. Paudel, U. Pan, R. Chising, M. Kandel, S. Prabhakaran, D. Kim, N. Kim and J. Lee, Applied Catalysis B: Environment and Energy, **2023**, 331, 122711.

[10] M. Ding, X. Hui and L. Yin, Electrochimica Acta, **2023**, 468, 142891.